Exchange bias study of sub-100 nm CoFeB/IrMn antidot and nanodot arrays fabricated by nanosphere lithography

X. Li[1], C. W. Leung[2], C.-C. Chiu[3], K.-W. Lin[3], M. Chan[4], Y. Zhou[5], Philip W. T. Pong[1, *]

[1] Department of Electrical and Electronic Engineering, The University of Hong Kong, Hong Kong

[2] Department of Applied Physics, The Hong Kong Polytechnic University, Hong Kong

[3] Department of Materials Science and Engineering, National Chung Hsing University, Taichung 402, Taiwan

[4] Department of Electronic and Computer Engineering, Hong Kong University of Science and Technology, Hong Kong

[5] Department of Physics, The University of Hong Kong, Hong Kong

* Tel: +852 28578491, Fax: +852 25598738, Email: ppong@eee.hku.hk

Abstract

Exchange-biased bilayers are widely used as reference layers in nanometric spintronic devices. While the magnetic properties of polycrystalline multilayers are widely reported, the exchange bias effect in nanostructures containing amorphous ferromagnetic layers are not systematically investigated. In this work, CoFeB/IrMn antidot and nanodot arrays were patterned by nanosphere lithography. The average diameter of pores in the antidot arrays changes from 88 nm to 105 nm as the thin film thickness increases from 20.8 nm to 28.5 nm, while the size of nanodots are kept at 60 nm. The exchange bias and coercivity of the nanostructures and continuous films exhibit similar exponential dependence on CoFeB layer thickness. The vacuum annealing under magnetic field results in structural relaxation, interdiffusion, and CoFeB crystallization, as the annealing temperature is increased from 373 K to 673 K. These mechanisms are responsible for the changes in crystallinity, surface roughness, and magnetic properties. Reduced coercivity and enhanced exchange bias is observed after annealing at low temperatures, while high-temperature annealing (> 573 K) results in higher coercivity and lower exchange bias. This work provides physical insights on the magnetization reversal response in nanosized spintronic devices involving CoFeB/IrMn reference layers.

Key words: exchange bias, nanostructures, nanosphere lithography

1. Introduction

The centers of hysteresis loops of ferromagnetic (FM) thin films shift away from zero when interfacing with antiferromagnetic (AF) layers [1], which is broadly known as the exchange bias effect. Benefited from the enhanced coercivity (H_c) and the loop shift (H_{ex}) [2], the exchange bias effect has brought great flexibility in tailoring the magnetization reversal properties of magnetic thin films, thus is used as reference layers in spin valves [3]. Ever since the primary discovery in CoO coated Co particles [4], intense research have been conducted to reveal the influencing factors of exchange bias, such as thin film composition [5], layer thickness [5, 6], applied field angle [7], field cooling [8, 9], ion-beam bombardment [10], and post annealing [11, 12].

The emergence of state-of-the-art micro- and nano-fabrication techniques accelerate the research and development on spintronic devices with ever shrinking dimensions, such as the nanometric magnetoresistive sensors, magnetic random access memories, and spin torque oscillators. Since the domain structures are altered by the reduced structural size, the exchange interactions in nanostructures differ greatly from those in continuous films [13, 14]. Both enhanced and reduced H_{ex} in nanostructures are reported, depending on the AF layer thicknesses [15-17] and structural sizes [18]. Most of the previous reports focus on the exchange-biased nanostructures with polycrystalline structures (such as CoFe/IrMn [13] and Co/IrMn [19]). CoFeB is an amorphous FM material which is widely used in magnetic tunnel junctions [20]. Both positive [21] and negative [22] H_{ex} are reported in CoFeB/IrMn planar films. However, the dependence of H_{ex} and H_c on CoFeB thickness in CoFeB/IrMn nanostructures remain unclear. Besides, CoFeB is partially crystallized after annealing [23], which may also result in changes in H_{ex}

and H_c. The investigation on the magnetic properties and annealing effect in CoFeB/IrMn nanostructures will be beneficial for understanding the magnetic switching properties in nanometric spintronic devices.

Nanosphere lithography (NSL) is a promising low-cost nanofabrication technique for patterning nanostructure arrays. The recent demonstration of magnetic nanodot [24-29] and antidot [30-32] structures and spin valve nanopillars [33] fabricated by NSL have proved its feasibility in patterning nanostructures for investigating magnetic properties. In this work, NSL is engaged for parallel fabrication of large-area CoFeB/IrMn nanodot and antidot arrays with diameters of less than 100 nm. The magnetic properties of continuous films, antidot, and nanodot arrays were compared and analyzed to study the influence of FM-layer thickness and annealing effect.

2. Experimental methods

The layer stack is Si/SiO_2/Ta 3.5/Ru 3.5/IrMn 8/CoFeB t_{FM}/Ta 3.5 (thickness in nanometers), in which t_{FM} is adjusted from 2 to 10 nm. High purity Ta, Cu, $Ir_{20}Mn_{80}$, $Co_{40}Fe_{40}B_{20}$, and Ru targets were DC-sputtered in argon pressure of 3×10^{-3} Torr at deposition rates ranging from 0.4 to 1 nm/min. An in-plane magnetic field of 30 mT was applied during the deposition.

The patterning process of nanodot and antidot arrays are similar to that in the references [24, 31, 34]. Detailed fabrication steps are shown in Figure 1. For the antidot arrays, the substrates were firstly cleaned and treated with positive electrolyte (0.2% water solution of Poly(diallyldimethylammonium chloride)) (Figure 1(a)). Non-close-packed polystyrene nanospheres (120 nm, negatively charged) were adsorbed to the wafer surface (Figure 1 (b)) by electrostatic interaction. Thin film stacks were subsequently sputtered on

the sphere masks while the substrate was rotating at 40 rpm ((Figure 1 (c)). During sputtering, the material gradually filled up the spaces between spheres, so the antidot diameter (d) increased with the thin film thickness (t) (Figure 1 (d)). The antidot arrays were formed (Figure 1 (e)) by lifting-off the spheres in toluene. For the nanodot arrays, the continuous films were firstly sputtered onto the rotating substrate (Figure 1 (f)). Then nanospheres were adsorbed to the film surface (Figure 1 (g)). Ar^+ ion milling were conducted while the sample was spinning at 37 rpm (Figure 1(h)). Since the ion beam was tilted by 45 degrees, the diameters of the nanodots were smaller than that of the spheres. Each sample was etched for 3 minutes at an overall etching rate of around 10 nm/min (the etch rate varies depending on the material). The nanodot arrays were formed by removing the residual spheres in toluene (Figure 1 (j)).

Samples with t_{FM} = 6 nm were vacuum annealed for 60 minutes under magnetic field of 0.15 T at 373 K to 673 K to investigate the annealing effect. The magnetization hysteresis loops of the as-deposited and annealed samples were measured at ambient temperature by a Microsense EZ7 vibrating sample magnetometer (VSM). The direction of the magnetic field during deposition and annealing were parallel to the positive direction of the VSM measurement. The planar and cross-sectional images were observed by a Hitachi S4800 field-emission scanning electron microscope (FE-SEM). The crystalline structures of the planar films were characterized by a Brüker AXS D8 Advance grazing incidence (0.5 degrees) X-ray diffraction (GIXRD) spectrometer. The surface morphologies of the planar films were characterized by a Parker XE-150 atomic force microscope (AFM) operating in tapping mode.

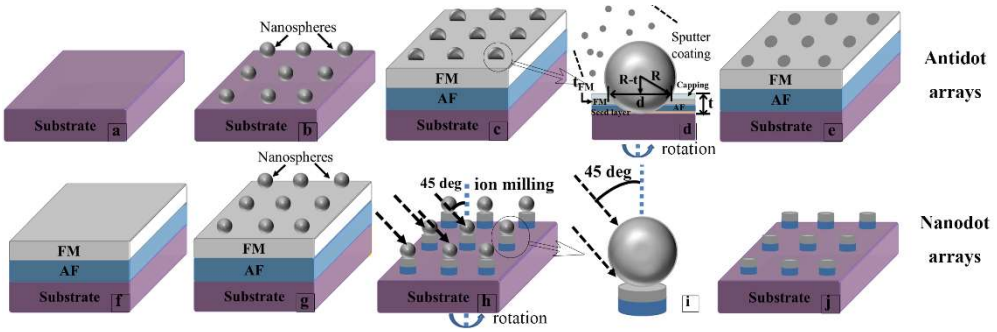

Figure 1 Fabrication procedures of antidot arrays ((a) – (e)) and nanodot arrays ((f) – (j)).

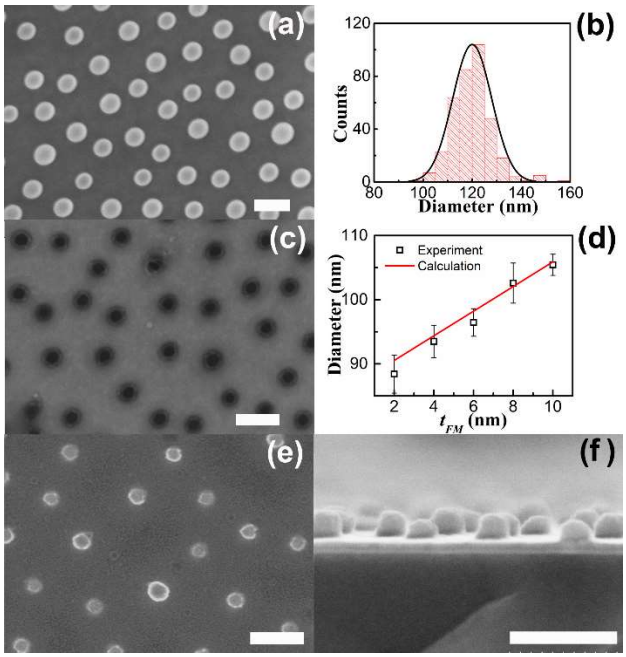

Figure 2 The surface morphologies of the samples characterized by SEM. (a) planar view of the nanospheres adsorbed on wafer surface; (b) the distribution histogram of the diameter of nanospheres; (c) planar view of the antidot arrays with t_{FM} = 8 nm; (d) square dot: the measured antidot diameter (scale bar refers to the 95% confidence interval of 30 samples); red line: the calculated d- t_{FM} relationship in equation (2); (e) planar view of the nanodot arrays with t_{FM} = 2 nm; (f) cross-sectional view of the nanodot arrays with t_{FM} = 2 nm. (Scale bar represents 200 nm)

3. Results and discussions

The surface morphologies of the samples are shown in Figure 2. Non-close-packed spheres are uniformly distributed (Figure 2(a)) with an average diameter of 120 nm (Figure 2(b)) and an average center-to-center distance of 220 nm. The planar view of antidot arrays with t_{FM} = 8 nm is presented in Figure 2(c). The radial distribution of the antidots duplicate that of the nanosphere masks, while the diameters are much smaller. From Figure 1(d), the thin film thickness ($t = t_{FM} + 18.5$ in this case) and the pore diameter (d) exhibit the following relation:

$$(\frac{d}{2})^2 + (R-t)^2 = R^2 \tag{1}$$

in which R = 60 nm is the diameter of the nanosphere. d can be roughly calculated through a Taylor linear approximation:

$$d = 1.92 t_{FM} + 86.7 \tag{2}$$

The measured diameters of pores correspond well with the calculations in equation (2), as shown in Figure 2(d). The top and cross-sectional views of the nanodot arrays are shown in Figures 2(e) and 2(f), respectively. The diameter of the dots with t_{FM} = 2 nm is reduced to around 60 nm in the tilted ion milling process. The 30-nm-thick dots observed by SEM is composed of multilayer stacks (t = 20.8 nm – 28.5 nm) and the over-etched substrate.

From the morphologies of the samples, we can conclude that regular nanostructures with lateral dimensions down to 60 nm can be fabricated by NSL. Based on this new method, the magnetic properties of CoFeB/IrMn exchange-biased nanostructures were investigated.

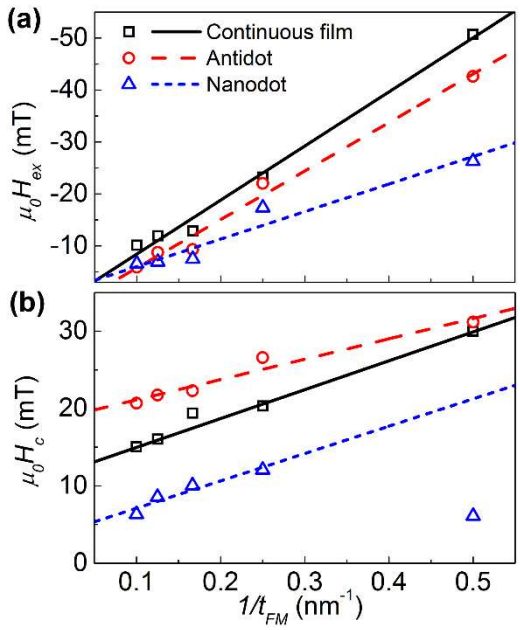

Figure 3 (a) H_{ex} and (b) H_c as a function of t_{FM} in continuous films, antidot and nanodot arrays respectively.

The H_{ex} and H_c of continuous films and nanostructures are plotted against $1/t_{FM}$ in Figures 3(a) and 3(b), respectively. As predicted by Stiles et al. [35-37], the H_{ex} and H_c of the continuous films exhibit exponential reliance on the FM thickness (t_{FM}):

$$H_{ex} \propto \frac{1}{t_{FM}^{m}} \tag{3}$$

$$H_{c} \propto \frac{1}{t_{FM}^{n}} \tag{4}$$

in which m and n are positive numbers, and approaches unity at room temperature. This relation is already reported in many experimental investigations on polycrystalline FM/AF pairs (such as Fe/MnF_2 [2], CoFe/IrMn [38], NiFe/FeMn [39] and NiFe/NiO [39]). The results in Figure 3 proves that H_{ex} and H_c of the continuous films and nanostructures of amorphous-CoFeB/IrMn also follow this $1/t_{FM}$ relation. It is noted that the H_c of the

nanodot arrays show some deviations from the linear fitting when t_{FM} = 2 nm. This can be explained by the increasing influence of the edge effect and defects when t_{FM} is small. The H_{ex} of the antidot arrays are smaller than that of the continuous films, which is contradictory to some previous observations [17]. However, this phenomena can be explained by the misaligned FM and AF spins at the edges of the pores [40]. In the meantime, the effect of reduced AF domain size, which is responsible for the enhance H_{ex} in antidot structures in the previous report [41], becomes marginal as the diameters of the antidots are reduced to smaller than 100 nm. Indeed, H_{ex} decreases at smaller pore diameter in NiFe/IrMn antidot arrays, as reported in the reference [42]. The smaller H_{ex} in nanodot arrays, on the other hand, is consistent with the previous report on 50-nm Co/IrMn nanodots [43]. The H_c of antidot arrays are larger than that of the continuous films, due to the enhanced domain wall pinning at the edge of the nanostructures in the FM and AF layers [13, 44]. The H_c of the nanodot array, on the other hand, is smaller than that of the continuous film, which is consistent with the previous report on Co/CoO nanodot arrays that H_{ex} and H_c decreases with reducing diameter [45]. This is possibly because of the reduction in thermal stability and the increasing influence of edge effects in the sub-100 nm nanodots.

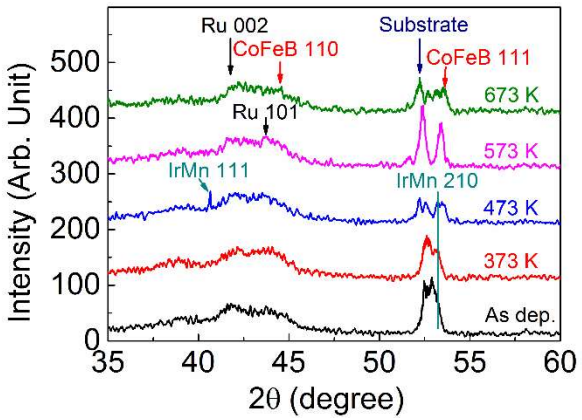

Figure 4 GIXRD patterns of the as-deposited and field-annealed continuous films.

In order to further investigate the structural changes induced by field annealing, the GIXRD patterns of as-deposited and annealed continuous films are shown in Figure 4. The as-deposited sample presents two broadened peaks at 2θ = 42.2° and 44.1°, corresponding to Ru (002) and (110) grains, respectively. The major peak at 2θ = 53° can be decomposed into one sub-peak at 2θ = 52.5° (which comes from the Si/SiO_2 substrate [46]) and another one at 2θ = 54° (which is contributed by IrMn (210)). As T_{an} increases to 473 K, a sharp IrMn (111) peak emerges at 2θ = 41.4°, indicating remarkable enhancement of crystallinity of IrMn. No diffraction peak of CoFeB crystallite is observed at T_{an} below 473 K, which confirms the amorphous structure of as-deposited CoFeB layer. Further increasing T_{an} results in body-centered cubic (BCC) CoFeB (111) texture, which is consistent with the previous report on the annealed CoFeB/Ru multilayers [47]. Meanwhile, the diffraction peaks of IrMn gradually vanishes, due to the detrimental effect of boron diffusion into IrMn at high annealing temperatures [48]. When T_{an} = 673 K, the broad diffused peak centered at 2θ = 45° evidences the formation of CoFeB (110) grains.

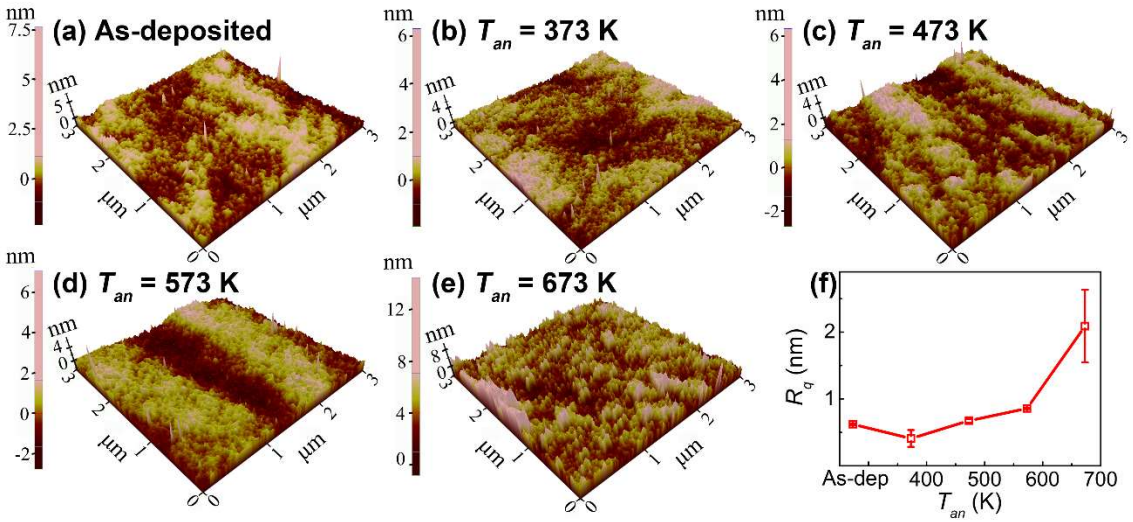

Figure 5 (a) – (e) AFM images (3 μm × 3 μm) and (f) RMS roughness measured on as-deposited and field annealed planar films (The error bars refer to the standard deviation of R_q measured on three regions).

The as-deposited and field-annealed continuous films were characterized by AFM, and the three-dimensional images and root mean square (RMS) roughness (R_q) at different T_{an} are shown in Figure 5. The roughness slightly decreases after 373 K field annealing. This indicates that the structural defects and disorders formed during deposition are relaxed during the low-temperature annealing. Further increasing T_{an} to 573 K results in a gradual increase in R_q, which is contributed by the grain growth with increasing T_{an} [49]. An abrupt increase in R_q and surface grain sizes occurs when T_a = 673 K. This is resulted from the interdiffusion of boron and Mn [50] and the crystallization of CoFeB, as evidenced by the reduction of IrMn crystallinity and the emergence of CoFeB diffraction peaks in Figure 4.

The changes in phases and structures in CoFeB/IrMn bilayers after annealing altered the magnetic properties of the continuous films, antidot and nanodot samples, as

shown in Figure 6. The hysteresis loops of the patterned nanostructures are more curved and less sharp than those of the continuous films, due to the pinning effect of edges and defects in nanostructures. The squareness of the hysteresis loops are increased after 100 °C annealing. This is because the density of defects in CoFeB is reduced after 100 °C annealing, as evidenced by the lower roughness characterized by AFM. The CoFeB layer switches more homogeneously when fewer pinning sites exist. Further increasing T_{an} results in reduced squareness, due to the enhanced diffusion at higher temperatures,

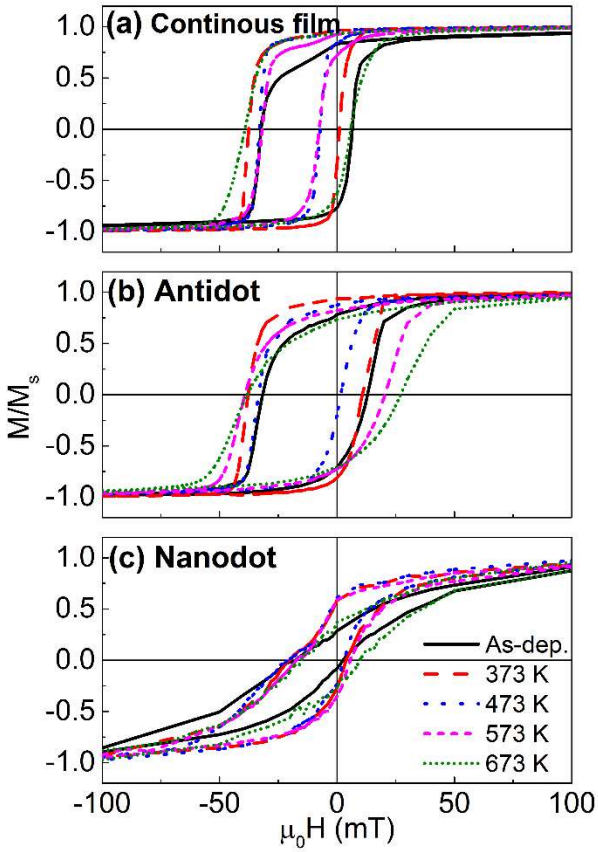

Figure 6 The magnetization hysteresis loops of as-deposited and field annealed (a) continuous films, (b) antidot arrays, and (c) nanodot arrays of CoFeB/IrMn exchange bias system with t_{FM} = 6 nm.

The H_{ex} and H_c of the antidot and nanodot arrays follow similar reliance on T_{an} as

the continuous films (Figure 7). The annealing temperature dependence of H_{ex} is closely correlated to the IrMn crystallinity shown in Figure 4. When $T_{an} < 473$ K, the H_{ex} increases with T_{an} due to the enhanced AF ordering in IrMn. When T_{an} is further increased to 673 K, the H_{ex} is remarkably reduced due to the loss of polycrystalline ordering in IrMn after high temperature annealing. H_c is slightly increased when $T_{an} = 373$ K, which is correlated to the enhanced H_{ex}. However, H_c is decreased when T_{an} is increased to 473 K or 573 K. The coexistence of high H_{ex} and low H_c at 473 K is attributed to the diffusion of Mn in CoFeB/IrMn interface. The resulted uncompensated interfacial spins in IrMn contributes to higher H_{ex} [22], while the diluted magnetic interface in CoFeB leads to lower H_c [21]. When $T_{an} = 673$ K, maximum H_c is achieved, due to the crystallization of CoFeB. The above results show that magnetic field annealing is effective in tailoring the microstructures and magnetic properties of exchange-biased multilayers.

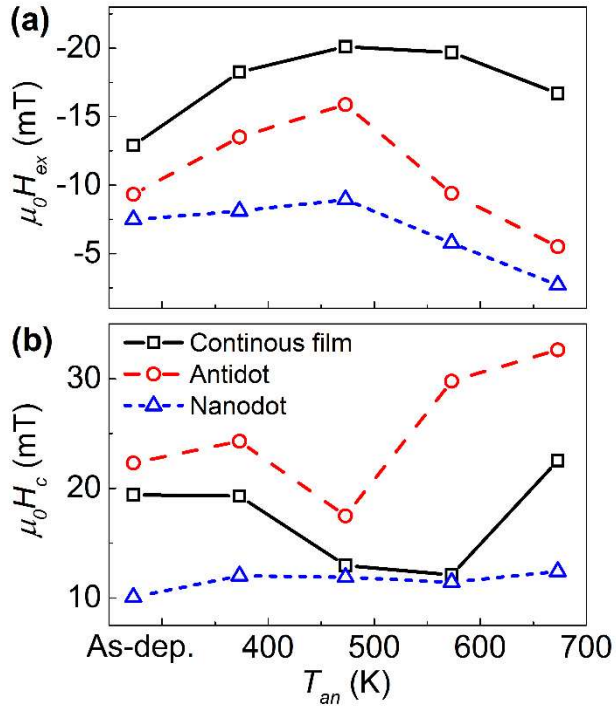

Figure 7 (a) H_{ex} and (b) H_c of the continuous films, antidot arrays, and nanodot arrays as a

function of T_{an} when t_{FM} = 6 nm.

4. Conclusions

The thickness dependence and annealing of the magnetic properties of CoFeB/IrMn continuous films and sub-100-nm nanostructures were investigated. The H_{ex} and H_c of the antidot, nanodot, and continuous films demonstrate similar $1/t_{FM}$ reliance on the amorphous-FM layer thickness as in polycrystalline multilayers. Field annealing at low temperature (T_{an} < 473 K) enhances the crystallization of IrMn, resulting in higher H_{ex}. Interdiffusion is promoted at higher annealing temperature, which leads to reduced IrMn crystallinity, increased surface roughness, and reduced H_{ex}. Both enhanced and reduced H_c are observed depending on T_{an}, due to the competing effect of exchange interaction and CoFeB crystallization (which increases H_c) and Mn diffusion (which reduces H_c). The results show that the exponential thickness dependence of H_{ex} and H_c can be extended to sub-100 nm nanostructures of amorphous-FM/AF bilayers. This work provides useful insight and guidance for the magnetic properties and microstructures of nanoscale spintronic devices containing CoFeB/IrMn reference layers.

Acknowledgement

This research is supported by the Seed Funding Program for Basic Research, Seed Funding Program for Applied Research and Small Project Funding Program from the University of Hong Kong, ITF Tier 3 funding (ITS-104/13, ITS-214/14), and University Grants Committee of HK (AoE/P-04/08). CWL acknowledges the support by PolyU (G-YM43/G-YBJ1)

References

[1] J. Nogués, I.K. Schuller, J. Magn. Magn. Mater., 192 (1999) 203.

[2] C. Leighton, M.R. Fitzsimmons, A. Hoffmann, J. Dura, C.F. Majkrzak, M.S. Lund, I.K. Schuller, Phys. Rev. B, 65 (2002) 064403.

[3] I.L. Prejbeanu, S. Bandiera, J. Alvarez-Hérault, R.C. Sousa, B. Dieny, J.P. Nozières, J Phys. D: Appl. Phys., 46 (2013) 074002.

[4] W.H. Meiklejohn, C.P. Bean, Phys. Rev., 105 (1957) 904-913.

[5] Jing-guo Hu, Guo-jun Jin, Y.-q. Ma, J. Appl. Phys., 92 (2002) 1009-1013.

[6] M. Ali, C.H. Marrows, M. Al-Jawad, B.J. Hickey, A. Misra, U. Nowak, K.D. Usadel, Phys. Rev. B, 68 (2003) 214420.

[7] T. Ambrose, R. L. Sommer, C.L. Chien, Phys. Rev. B, 56 (1997) 83.

[8] K.W. Lin, M.R. Wei, J.Y. Guo, J. Nanosci. Nanotechnol., 9 (2009) 2023.

[9] X. Li, K.W. Lin, H.Y. Liu, D.H. Wei, G.J. Li, P.W.T. Pong, Thin Solid Films, 570 (2014) 383-389.

[10] K.W. Lin, M. Mirza, C. Shueh, H.R. Huang, H.F. Hsu, J. van Lierop, Appl. Phys. Lett., 100 (2012) 122409.

[11] A.C. Sun, H.F. Hsu, H.J. Wu, J.H. Hsu, P.W.T. Pong, T. Suzuki, K.W. Lin, IEEE Trans. Magn., 47 (2011) 501.

[12] T. Yu, H. Naganuma, W.X. Wang, Y. Ando, X.F. Han, J. Appl. Phys., 111 (2012) 07D908.

[13] M.T. Rahman, N.N. Shams, D.S. Wang, C.-H. Lai, Appl. Phys. Lett., 94 (2009) 082503.

[14] A. Sharma, S.Tripathi, K.C.Ugochukwu, J. Magn. Magn. Mater., 326 (2013) 97.

[15] V. Baltz, J. Sort, S. Landis, B. Rodmacq, B. Dieny, Phys. Rev. Lett., 94 (2005) 117201.

[16] W.J. Gong, W. Liu, J.N. Feng, D.S. Kim, C.J. Choi, Z.D. Zhang, J. Appl. Phys., 115 (2014) 133909.

[17] D. Tripathy, A.O. Adeyeye, J. Appl. Phys., 105 (2009) 07D703.

[18] K. Temst, E. Girgis, R.D. Portugal, H. Loosvelt, E. Popova, M.J.V. Bael, C.V. Haesendonck, H. Fritzsche, M. Gierlings, L.H.A. Leunissen, R. Jonckheere, Eur. Phys. J. B., 45 (2005) 261.

[19] G. Vinai, J. Moritz, G. Gaudin, J. Vogel, M. Bonfim, F. Lançon, I.L. Prejbeanu, K. Mackay, B. Dieny, J Phys. D: Appl. Phys., 46 (2013) 345308.

[20] S. Ikeda, J. Hayakawa, Y. Ashizawa, Y.M. Lee, K. Miura, H. Hasegawa, M. Tsunoda, F. Matsukura, H. Ohno, Appl. Phys. Lett., 93 (2008) 082508.

[21] M. Raju, S. Chaudhary, D.K. Pandya, The European Physical Journal B - Condensed Matter and Complex Systems, 86 (2013) 491.

[22] A. Kohn, J. Dean, A. Kovacs, A. Zeltser, M.J. Carey, D. Geiger, G. Hrkac, T. Schrefl, D. Allwood, J. Appl. Phys., 109 (2011) 083924.

[23] S. Yuasa, Y. Suzuki, T. Katayama, K. Ando, Appl. Phys. Lett., 87 (2005) 242503.

[24] L. Balcells, B. Martinez, O. Iglesias, J.M. García-Martín, A. Cebollada, A. García-Martín, G. Armelles, B. Sepúlveda, Y. Alaverdyan, Appl. Phys. Lett., 94 (2009) 062502.

[25] J.B. González-Díaz, A. García-Martín, J.M. García-Martín, A. Cebollada, G. Armelles, B. Sepúlveda, Y. Alaverdyan, M. Käll, Small, 4 (2008) 202.

[26] S.M. Weekes, F.Y. Ogrin, W.A. Murray, P.S. Keatley, Langmuir, 23 (2006) 1057.

[27] X. Li, Z.R. Tadisina, S. Gupta, G. Ju, J. Vac. Sci. Technol A, 27 (2009) 1062-1066.

[28] P. Tiberto, G. Barrera, L. Boarino, F. Celegato, M. Coisson, N. De Leo, F. Albertini, F. Casoli, P. Ranzieri, J. Appl. Phys., 113 (2013) 17B516.

[29] P. Tiberto, L. Boarino, F. Celegato, M. Coisson, E. Enrico, N. de Leo, F. Vinai, P. Allia, J. Nanopart. Res., 13 (2011) 4211.

[30] M. Coïsson, L. Boarino, F. Celegato, N. Leo, P. Tiberto, F. Vinai, J. Nanopart. Res., 13 (2011) 5641.

[31] C.-C. Ho, T.-W. Hsieh, H.-H. Kung, W.-T. Juan, K.-H. Lin, W.-L. Lee, Appl. Phys. Lett., 96 (2010) 122504.

[32] P. Tiberto, L. Boarino, F. Celegato, M. Coisson, N. De Leo, F. Vinai, P. Allia, J. Appl. Phys., 107 (2010) 09B502.

[33] W.G. Wang, A. Pearse, M. Li, S. Hageman, A.X. Chen, F.Q. Zhu, C.L. Chien, Sci. Rep., 3 (2013) 01948.

[34] P. Hanarp, D.S. Sutherland, J. Gold, B. Kasemo, Colloids Surf., A Physicochem. Eng. Asp., 214 (2003) 23-36.

[35] M.D. Stiles, R.D. McMichael, Phys. Rev. B, 60 (1999) 12950.

[36] M.D. Stiles, R.D. McMichael, Phys. Rev. B, 59 (1999) 3722-3733.

[37] M.D. Stiles, R.D. McMichael, Phys. Rev. B, 63 (2001) 064405.

[38] H. Li, P.P. Freitas, Z. Wang, J.B. Sousa, P. Gogol, J. Chapman, J. Appl. Phys., 89 (2001) 6904.

[39] T. Lin, T. Ching, R.E. Fontana, J.K. Howard, IEEE Trans. Magn., 31 (1995) 2585.

[40] J. Changjun, X. Desheng, F. Xiaolong, G. Dangwei, L. Qingfang, Nanotechnology, 18 (2007) 335703.

[41] A.P. Malozemoff, Phys. Rev. B, 35 (1987) 3679-3682.

[42] D. Tripathy, A.O. Adeyeye, N. Singh, Appl. Phys. Lett., 93 (2008) 022502.

[43] G. Vinai, J. Moritz, G. Gaudin, J. Vogel, M. Bonfim, F. Lançon, I.L. Prejbeanu, K. Mackay, B. Dieny, J. Phys. D: Appl. Phys., 46 (2013) 345308.

[44] D. Tripathy, A.O. Adeyeye, J. Appl. Phys., 105 (2009) -.

[45] E. Girgis, R.D. Portugal, H. Loosvelt, M.J. Van Bael, I. Gordon, M. Malfait, K. Temst, C. Van Haesendonck, L.H.A. Leunissen, R. Jonckheere, Phys. Rev. Lett., 91 (2003) 187202.

[46] G.V. Swamy, H. Pandey, A.K. Srivastava, M.K. Dalai, K.K. Maurya, Rashmi, R.K. Rakshit, AIP Adv., 3 (2013) 072129.

[47] D.J. Kim, J.Y. Bae, W.C. Lim, K.W. Kim, T.D. Lee, J. Appl. Phys., 101 (2007) 09B505.

[48] J. Hayakawaa, S. Ikeda, Y.M. Lee, F. Matsukura, H. Ohno, Appl. Phys. Lett., 89 (2006).

[49] A. Gupta, S. Mohanan, M. Kinyanjui, A. Chuvilin, U. Kaiser, U. Herr, J. Appl. Phys., 107 (2010) 093910.

[50] S. Cardoso, P.P. Freitas, Z.G. Zhang, P. Wei, N. Barradas, J.C. Soares, J. Appl. Phys., 89 (2001) 6650-6652.

[51] J. Tang, K.-Y. Wang, W. Zhou, J. Appl. Phys., 89 (2001) 7690-7692.